ANIMAL LOCOMOTION

Agile and versatile climbing on ferromagnetic surfaces with a quadrupedal robot

Seungwoo Hong[1]†, Yong Um[1]†, Jaejun Park[2], Hae-Won Park[1]*

A climbing robot that can rapidly move on diverse surfaces such as floors, walls, and ceilings will have an enlarged operational workspace compared with other terrestrial robots. However, the climbing skill of robots in such environments has been limited to low speeds or simple locomotion tasks. Here, we present an untethered quadrupedal climbing robot called MARVEL (magnetically adhesive robot for versatile and expeditious locomotion), capable of agile and versatile climbing locomotion in ferromagnetic environments. MARVEL excels over prior climbing robots in terms of climbing speed and ability to execute various motions. It demonstrates the fastest vertical and inverted walking speed, whereas its versatile locomotion ability enables the highest number of gaits and locomotion tasks. The key innovations are an integrated foot design using electropermanent magnets and magnetorheological elastomers that provide large adhesion and traction forces, torque control actuators, and a model predictive control framework adapted for stable climbing. In experiments, the robot achieved locomotion on ceilings and vertical walls up to 0.5 meter (1.51 body lengths) per second and 0.7 meter (2.12 body lengths) per second, respectively. Furthermore, the robot exhibited complex behaviors such as stepping over 10-centimeter-wide gaps; overcoming 5-centimeter-high obstacles; and making transitions between floors, walls, and ceilings. We also show that MARVEL could climb on a curved surface of a storage tank covered with up to 0.3-millimeter-thick paint with rust and dust.

INTRODUCTION

Numerous industrial operations (such as inspections of storage tanks, bridges, and shipyards) are carried out in ferromagnetic environments that contain gaps, protuberances, corners, walls, and ceilings. In many cases, these operating environments are difficult and even dangerous for human operators to directly access. Legged robots could potentially perform various maneuvers in such confined and complex three-dimensional (3D) environments. To robustly and rapidly traverse such real-world scenarios, the legged robots must have appropriate adhesion mechanisms, leg morphology, and actuation schemes as well as controllers that can produce multiple modes of locomotion, such as vertical and inverted locomotion, as well as obstacle overcoming and plane-to-plane transitions. These design components are inherently coupled and vary depending on factors such as the purpose and function of a robot and the nature of the terrain. Foremost among the design components is the adhesion mechanism, which provides holding force to facilitate locomotion against the force of gravity. Legged climbing robots have been developed with different types of adhesion mechanisms, including pneumatic [active suction (*1*–*3*) and passive suction cups (*4*)], mechanical [grippers (*5*–*7*) and frictional contact (*8*–*10*)], bioinspired (*11*–*19*), electroadhesive (*20*, *21*), and magnetic-based approaches (*22*–*29*), each serving a particular purpose and applicable to different surfaces. The most commonly adopted adhesion mechanism is pneumatic adhesion, such as active suction using vacuum pumps (*1*–*3*) and passive suction cups (*4*) that are effective on smooth surfaces regardless of materials; however, high energy consumption required for vacuum pumps and the time delay caused by pressurizing the suction cups limit their application for autonomously powered, legged locomotion.

Biologically inspired adhesion is an attractive option for agile legged locomotion on vertical surfaces; such mechanisms take a short time to generate holding forces and consume zero static energy while adhered to substrates. Stickybot (*11*) uses gecko-inspired design principles involving hierarchical conformability and anisotropic adhesion and can climb on smooth vertical surfaces at speeds of up to 0.04 m/s (0.12 body lengths/s). The SpinybotII (*12*, *13*) and RiSE (*14*–*17*) platforms use compliant microspines adapted from the spine structures of insects and can effectively scale and cling to various hard and porous vertical surfaces. Similar spine or claw-like mechanisms have been used for high-speed climbing locomotion on porous or penetrable surfaces. RiSE V3 (*17*) can climb on a cylindrical structure at speeds of up to 0.21 m/s (0.3 body lengths/s), CLASH (*18*) can climb on fabric at speeds of up to 0.15 m/s (1.5 body lengths/s), and DynoClimber (*19*) can scale a vertically mounted carpet at a maximum speed of 0.67 m/s (1.675 body lengths/s). However, despite their climbing performance on vertical surfaces, they have not been thoroughly investigated for overcoming obstacles and turning or for applicability to inverted surfaces.

Other approaches, such as electroadhesion and magnetic-based adhesion, have been successfully applied for versatile legged locomotion on both vertical and inverted surfaces. HAMR-E (Harvard Ambulatory MicroRobot with Electroadhesion) (*20*) robot uses electroadhesion pads and can effectively locomote on various terrains ranging from smooth to curved surfaces. This type of adhesion has the advantages of being lightweight, energy efficient, and surface independent; however, because of its low holding pressure, for example, 42.4 kPa in the normal (or 14 kPa in the shear) direction on steel surfaces with 4000-V dc actuation voltage as reported in (*21*), which necessitates large contact areas

---

[1]Department of Mechanical Engineering, Korea Advanced Institute of Science and Technology, 291, Daehak-ro, Yuseong-gu, Daejeon 34141, Republic of Korea. [2]Department of Mechanical Science and Engineering, University of Illinois at Urbana-Champaign, Urbana, IL, USA.
*Corresponding author. Email: haewonpark@kaist.ac.kr
†These authors contributed equally to this work.

to generate adequate holding forces, electroadhesion is thus only suitable for millimeter-scale legged robots. Another family of climbing robots is equipped with magnetic footpads that provide high holding pressure on ferromagnetic surfaces. The mechanism used for attachment and detachment of magnetic foot determines the overall design complexity and power consumption of the robot. For instance, permanent magnet–based mechanisms (*22*–*24*) require the robot to attach (or detach) magnetic feet on the substrate using additional mechanical actuators that increase the overall weight and attachment (or detachment) time. Electromagnets (*25*–*27*) do not require any mechanical parts and can realize fast attachment (or detachment) by switching on (or off) the electric current; however, electromagnets have the disadvantage of high power consumption that requires a continuous power supply to retain the holding force. To overcome these drawbacks, electropermanent magnetic (EPM) footpads have been adopted by a few robots (*28*, *29*) to realize versatile mobility on both vertical and inverted surfaces made of ferromagnetic materials. An EPM is a two-state switchable device that can change its magnetic state by electric currents. The two states are the state of being magnetized, which produces magnetic force, and the state of being demagnetized, where no magnetic force remains. Unlike electromagnets, no energy is needed to maintain the state of the EPM. The EPM device provides holding pressure in the normal direction larger than those of other adhesion methods; however, the EPM has low holding pressure in the shear direction because of the low coefficient of friction of steel. This hinders the performance of dynamic maneuvers in the vertical direction, where a large shear holding force is required to climb against the force of gravity.

Here, we present an untethered quadrupedal climbing platform, MARVEL (magnetically adhesive robot for versatile and expeditious locomotion) (Movie 1), which can dynamically move on ferromagnetic walls (Fig. 1A) and ceilings (Fig. 1B) as well as traverse gaps and obstacles (Fig. 1C), perform plane-to-plane transitions (Fig. 1D), traverse on the storage tank (Fig. 1E), and carry a payload (Fig. 1F). To enable versatile dynamic motions of the proposed platform, we developed a synthetic magnetic foot design that combines an EPM design to realize high energy efficiency and fast switching time and a design of magnetorheological elastomer (MRE) footpads to provide large holding pressure in both shear and normal directions. Because of its compact and lightweight design, MARVEL can seamlessly integrate synthetic magnetic feet with the widely adopted proprioceptive actuation scheme (*30*, *31*), which has high torque transparency and backdrivability. The integration of this actuation scheme allows not only contact force control without the use of a force sensor but also compliant interaction with the surroundings to handle contact impacts. Using this contact force control capability, a reliable controller can enable dynamic locomotion; in the presence of physical constraints, optimally distributed ground reaction forces (GRFs) can prevent slipping and tipping over during foot adhesion to substrates.

RESULTS

MARVEL description

MARVEL is an 8-kg dynamic and versatile climbing quadruped robot with four 0.2-kg magnetic feet (Fig. 2A). Figure 2 (B and C) shows the overall electronic architecture and design components of MARVEL with magnetic feet, leg modules, torso, and electronics (details about electronics are explained in the Supplementary Materials). The leg modules are driven by proprioceptive actuators and were manufactured on the basis of the design proposed in (*32*), where a design of the leg prototype was suggested considering a balance between torque and speed of motor for dynamic locomotion. Adopting the actuator design from (*32*), we designed a climbing quadruped robot with mammal-type leg morphology, allowing the robot to achieve both agility and a large foot workspace for versatility. The torso is designed to contain all electronics for untethered operations. The width, height, and length of the torso are 119, 131, and 330 mm (from the frontal hip joint to the rear hip joint), respectively.

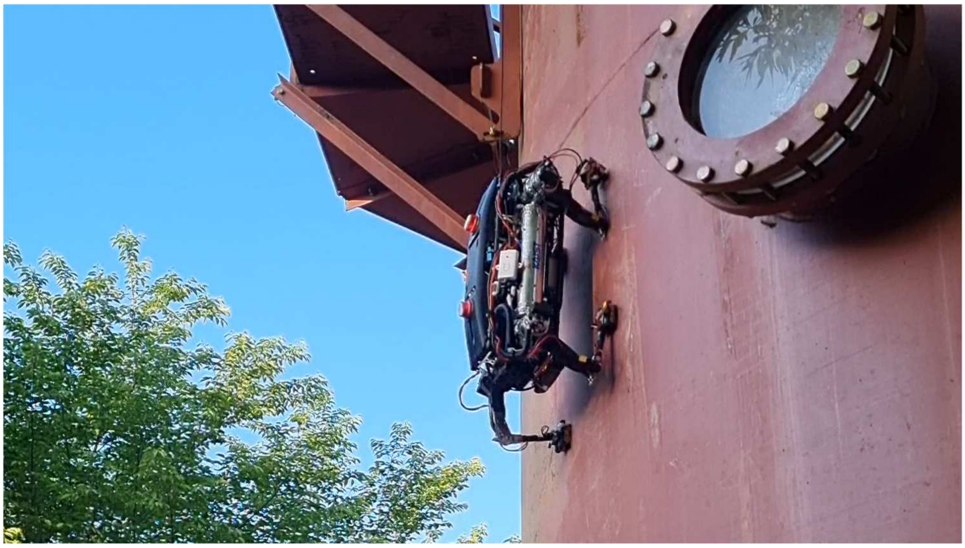

Movie 1. Summary video explaining agile and versatile climbing with MARVEL.

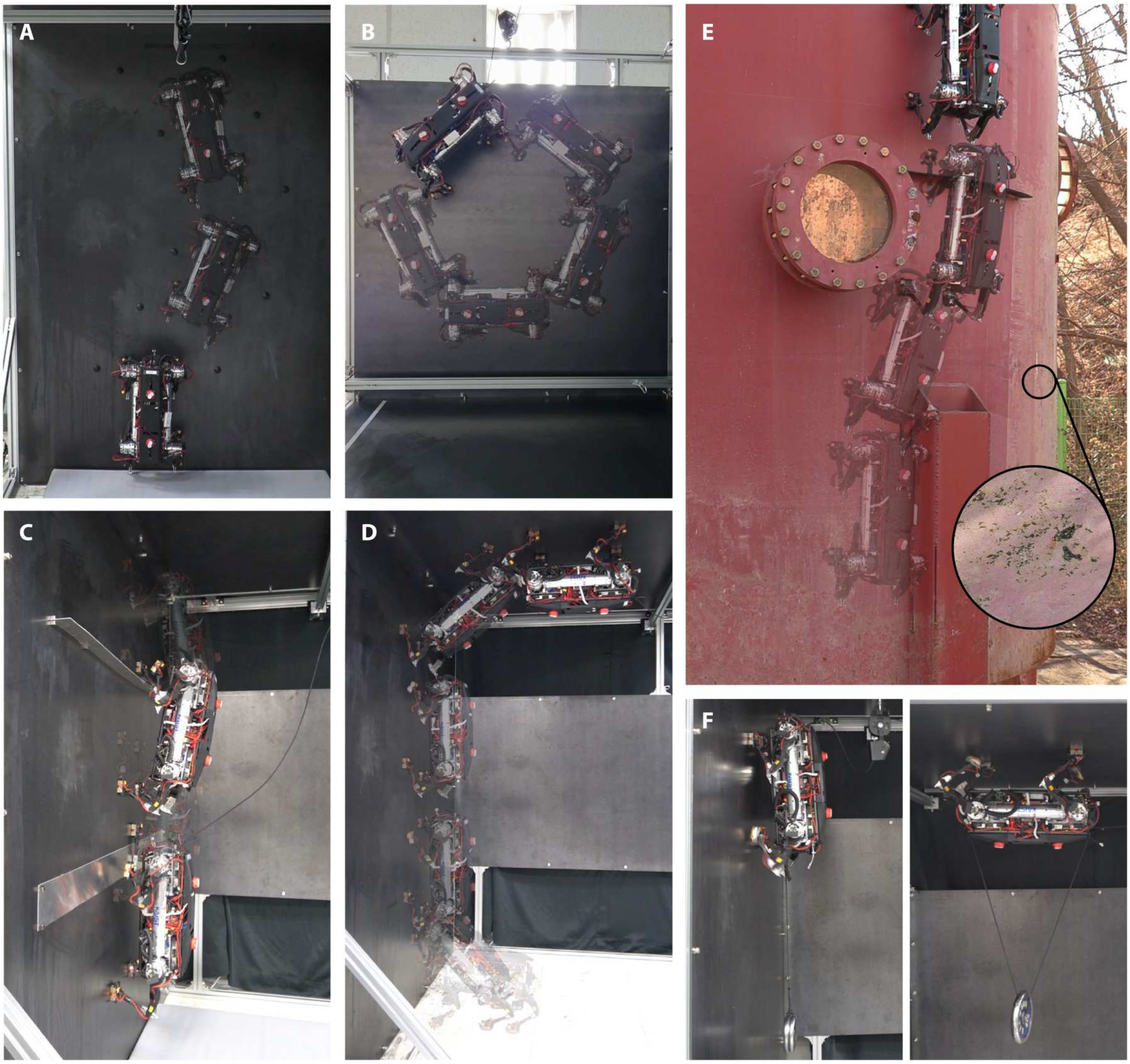

Fig. 1. MARVEL performing various locomotion tasks. (**A**) Turning movement on a vertical wall. (**B**) Turning movement on a ceiling. (**C**) Traversing a gap (10 cm) and an obstacle (5 cm). (**D**) The transition from floor to wall and from wall to ceiling. (**E**) Vertical locomotion on a storage tank, where the surface is covered with paint, rust, and dust. (**F**) Carrying (left) a 2-kg payload on a wall and (right) a 3-kg payload on a ceiling.

Design of magnetic foot for dynamic and versatile climbing locomotion

For dynamic and versatile climbing locomotion, a robotic foot should have sufficient holding forces in both normal and shear directions, an instantaneous switching of holding forces, high energy efficiency, and robust and compliant attachment to the substrate. As mentioned in Introduction, we developed a magnetic foot that combines an EPM and an MRE; this magnetic foot was incorporated with the leg module using a low-height, three–degrees of freedom (DOFs) compliant passive ankle (Fig. 3A). The following sections describe how these components can achieve synergistic effects and satisfy the aforementioned four requirements.

Low-voltage and fast switchable EPMs with high energy efficiency

For faster switching and lower energy consumption than previously reported EPMs in (*33*–*37*), an EPM geometry was proposed. In prior parallel-structured EPMs (P-EPMs), the coil for reversing the magnetization direction of a semihard magnet surrounded both core magnets such that the length of the coil wire increased unnecessarily. This increased the coil resistance and eventually the voltage required for switching, necessitating heavy batteries or an additional voltage converter. To solve this problem, we separated the core magnets into a square structure and wound the coil only around the semihard magnet. As a result, we were able to decrease the minimum switching voltage, allowing square-structured EPMs (S-EPMs) to perform faster and more energy-efficient switching than P-EPM. The structure and components of the S-EPM are illustrated in Fig. 3B. The dimensions in Fig. 3B are based on the S-EPM designed in this study. The working principle of the S-EPM is illustrated in Fig. 3C.

Figure 4 (A and B) compares the holding force and the switching characteristics of S-EPMs and P-EPMs from the magnetic circuit analysis provided in the Supplementary Materials with respect to

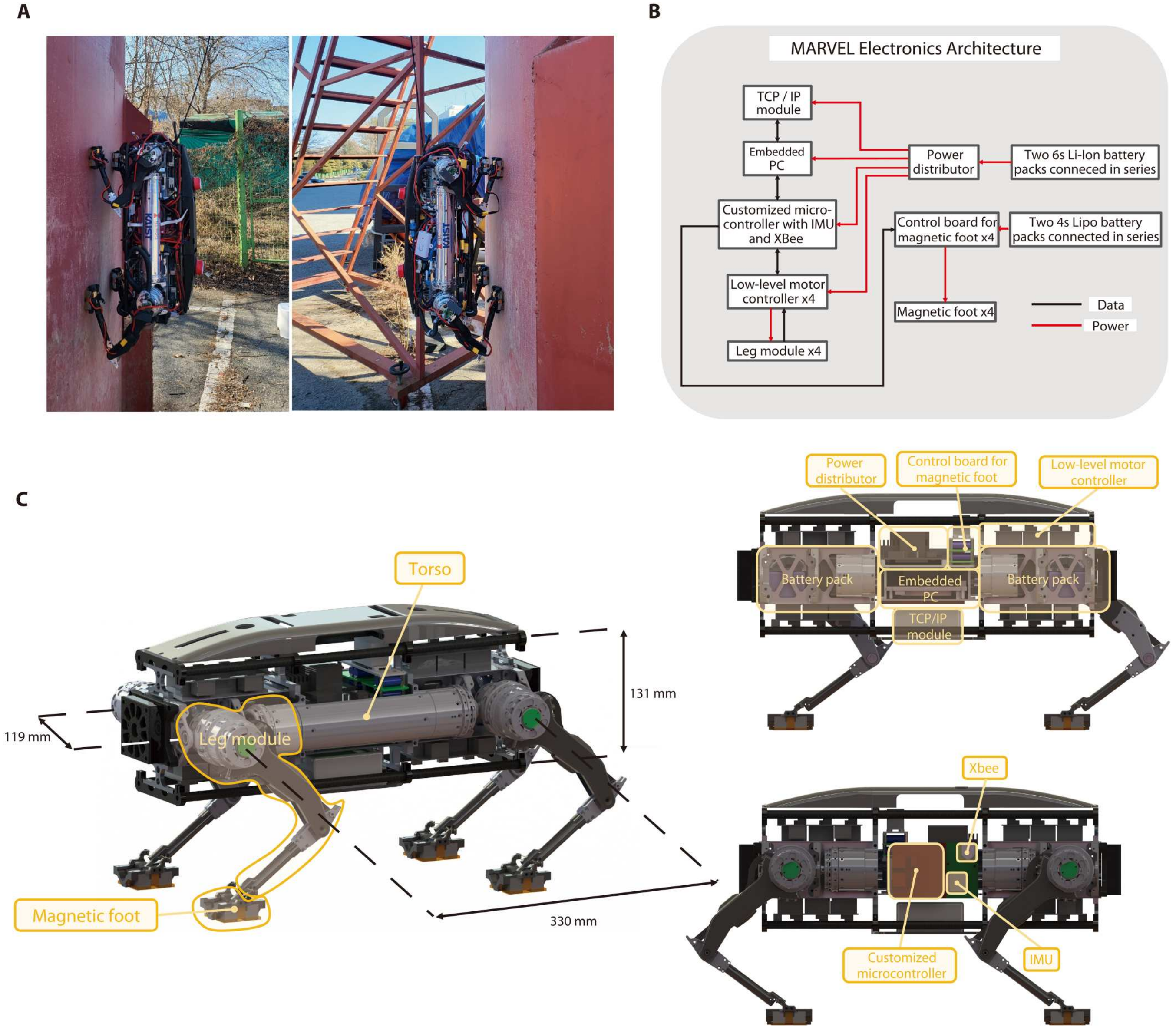

Fig. 2. MARVEL description. (**A**) MARVEL clinging to a steel storage tank. (**B**) MARVEL electronic architecture. (**C**) Mechanical and electronic components of MARVEL.

the width (w_m) and the aspect ratio ($\gamma = L_m/w_m$) of the core magnet. As shown in Fig. 4A, the S-EPM without the MRE footpad has the same holding force as the P-EPM. However, in terms of switching characteristics, S-EPMs have a lower minimum switching voltage, switching time, and energy than P-EPMs at the same magnet width and aspect ratio (Fig. 4B). Figure 4A also shows a holding force analysis of the S-EPM with the MRE footpad. As the MRE footpad increases the coefficient of friction, the S-EPM has larger shear holding force than the S-EPM without the MRE footpad. Hence, despite the decrease in normal holding force, the maximum amounts of normal and shear holding forces that the footpad can generate become similar. This balanced amount of normal and shear holding force can be beneficial when walking capabilities on vertical and inverted surfaces are both important. The analysis in Fig. 4 (A and B) also reveals that increasing the width and the aspect ratio will increase the holding forces, but this will result in higher minimum switching voltage, switching energy, and time. Therefore, the design choice of balancing holding forces and desirable switching characteristics should be made. In this research, the design parameters were selected considering the required switching characteristics and holding force, the overall size and weight of the robot (Fig. 3B), and the available sizes of the off-the-shelf magnets on the market. The details of the design parameters and the analysis are provided in the Supplementary Materials.

The proposed S-EPM requires 5 ms to switch its state. This switching time accounts for 2% of stance time when MARVEL performs gaits with the stance and swing time of 250 ms. Note that the switching time is comparable with that of geckos in nature: A gecko can attach one of its adhesive pads in 5 ± 2 ms and detach it in 15 ± 4 ms on average, as reported in (*38*). To switch the S-EPM, a voltage

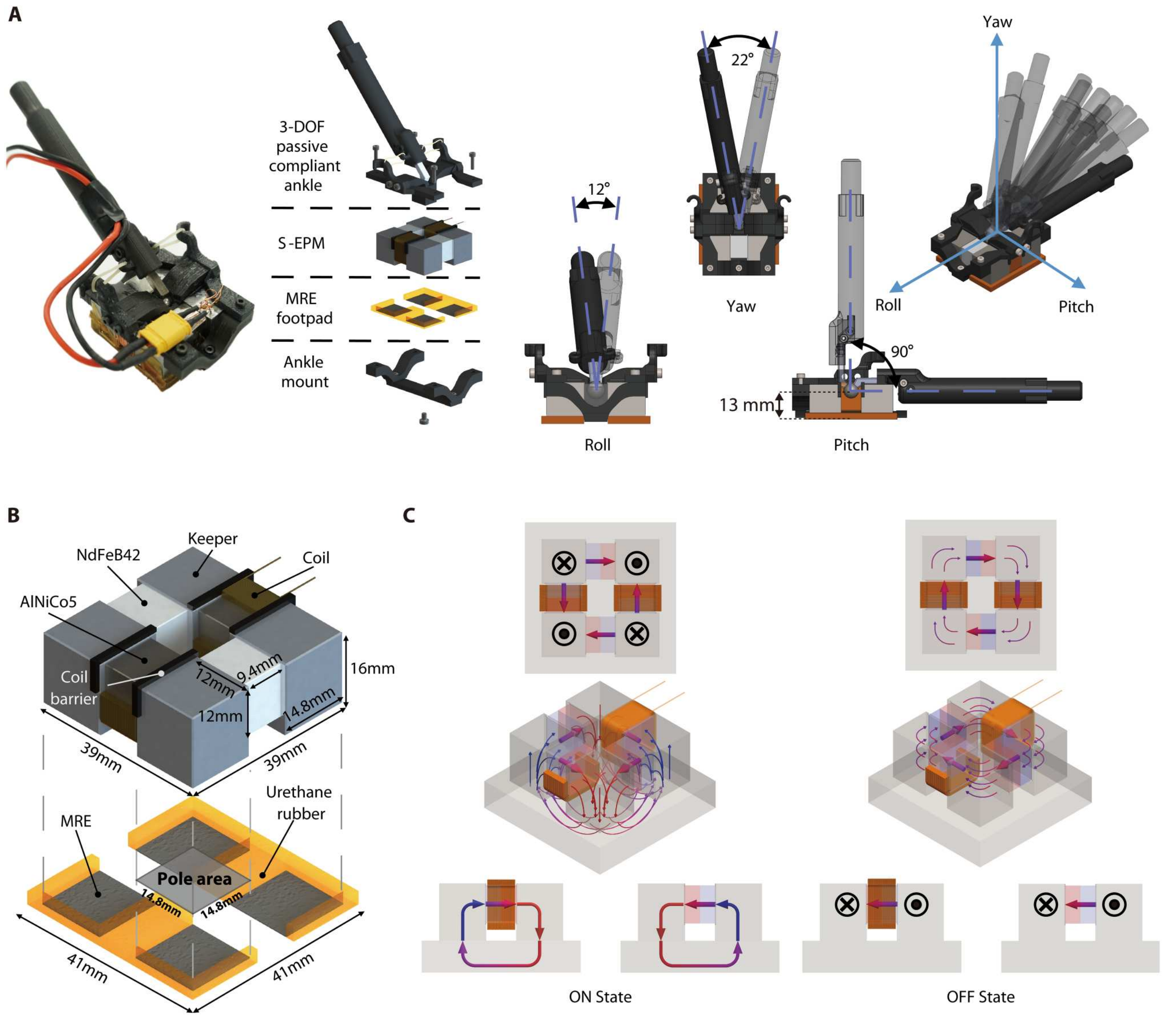

Fig. 3. Magnetic foot description. (**A**) Components of the magnetic foot. A magnetic foot consists of the ankle, the S-EPM, and the MRE footpad. The ankle joint is shown with its allowable leg rotation angle. (**B**) Components of the S-EPM and MRE footpad. Two cuboid AlNiCo5 (semihard) and two cuboid NdFeB42 (hard) magnets were selected as core magnets. Keepers are made of pure iron and keep core magnets fixed in a square structure. Because MREs have excellent friction characteristics and high permeability, an MRE was used as a footpad for the magnet foot. (**C**) Working principle of the S-EPM. If the magnetization direction of AlNiCo5 is aligned as shown on the left, then the magnetic flux comes out of the keeper and circulates through the steel plate to produce a holding force (ON state). Conversely, if the magnetization direction of AlNiCo5 in the direction is aligned as shown on the right, then the magnetic flux circulates inside the S-EPM, and the holding force disappears (OFF state).

pulse must be supplied until the coil current reaches a value that can reverse the magnetization direction of the AlNiCo magnet. Here, on the basis of the analysis of the S-EPM electrical characteristics (given in the Supplementary Materials), a voltage pulse of 29.6 V over 5 ms was applied to the coils. Figure 4C shows the current and voltage response of the S-EPM after the voltage pulse was applied to the coils. As shown in Fig. 4C, the voltage pulse measured 26.6 to 28.6 V over 5 ms; the current reached a peak of 36.8 A. Although the measured voltage pulse was about 1 to 3 V lower than the desired value of 29.6 V, this voltage pulse can provide sufficient current to saturate the AlNiCo magnet and allow the proposed S-EPM to produce a maximum holding force, as shown in Fig. 4D. Switching energy, 4.07 J, was obtained by numerical integration of the power over the switching time. The proposed magnetic foot requires voltage and current of 29.6 V and 35.18 A, respectively, so a lightweight power source can perform switching of S-EPMs. As a power source for the magnetic foot, two Nanotech 850-mAh 4S 45~90C LiPo (lithium polymer) packs were connected in series. The power system, including a battery and four control boards for the magnetic feet, weighed about 240 g and could be installed in the torso of MARVEL. On the basis of the given values of energy consumption and battery capacity, the magnetic foot can be switched ON and OFF up to about 22,255 times, enabling 2781 walking steps.

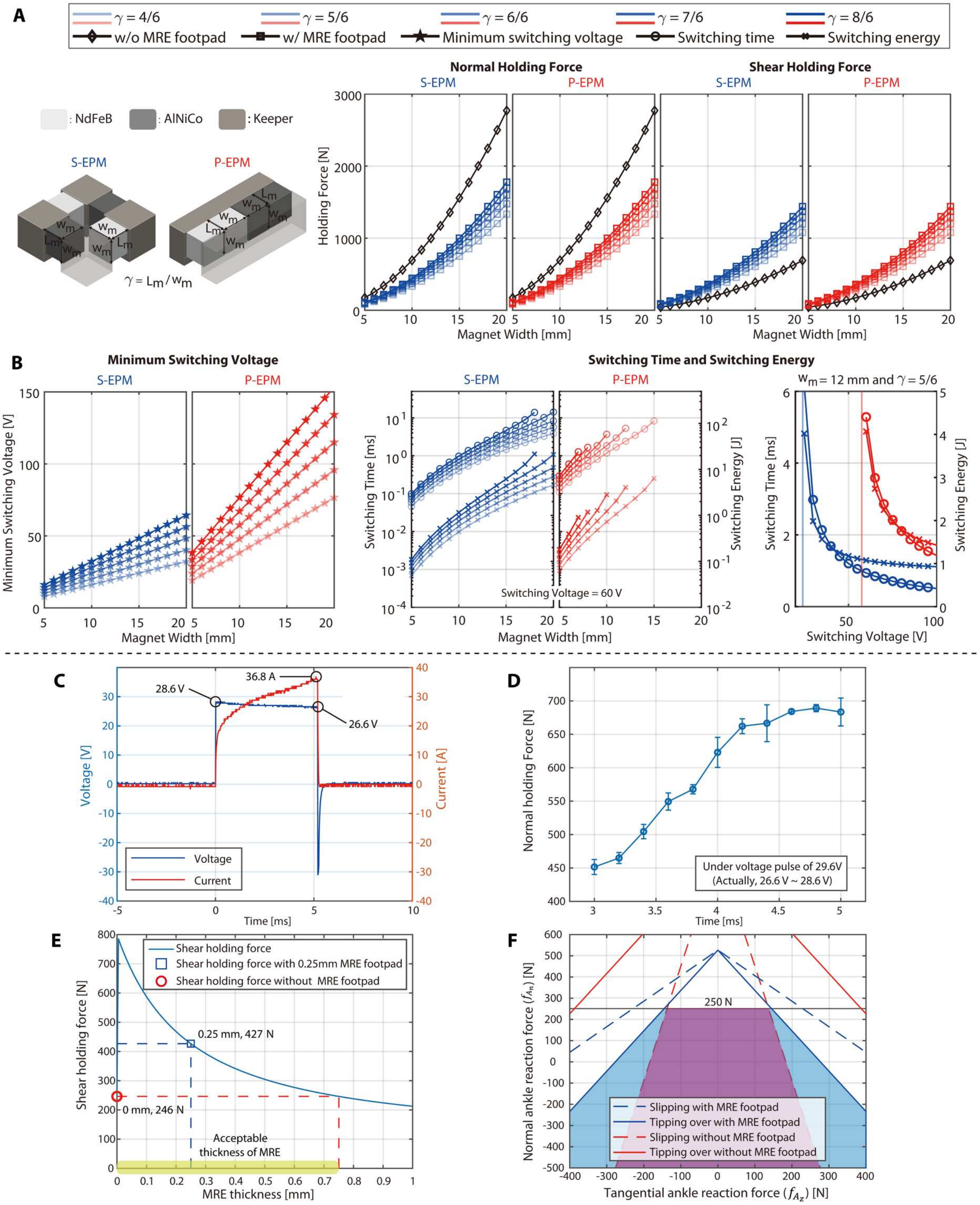

Fig. 4. Holding force and switching characteristics of the S-EPM and the P-EPM and the admissible ankle reaction force region. (**A**) Holding force of the S-EPM with and without the MRE footpad and the P-EPM. For the case without the MRE footpad, the holding force does not vary with γ values (black lines with diamond markers). (**B**) Minimum switching voltage, switching time, and energy of the S-EPM and P-EPM. (**C**) Voltage and current response of the S-EPM. (**D**) Normal holding force of the S-EPM with respect to pulse time (means ± SD, three trials). After about 4.6 ms, the holding force saturates and reaches its maximum value. (**E**) Shear holding force with respect to the MRE thickness. (**F**) The region of admissible ankle reaction forces.

MRE as nonslippery footpad for magnetic foot

Locomotion on vertical and inverted surfaces requires foot adhesion mechanisms with a large holding force in the shear and normal directions. The shear holding force can be described by Coulomb friction, $F_{\text{shear}} = \mu F_{\text{normal}}$, where F_{shear} is the shear holding force, F_{normal} is the normal holding force, and μ is the coefficient of friction between the adhesion mechanism and the substrate. Because the contact surface is usually slippery machined steel for magnetic adhesion, the coefficient of friction is relatively lower than that of surfaces between rubber and steel. To increase friction, many legged robots have used polyurethane or rubber footpads (*39*–*43*). However, these footpads act as air gaps, substantially reducing the holding force in the normal direction and thereby decreasing the holding force in the shear direction.

To tackle this problem, we used MREs as footpads of the magnetic foot. An MRE is a class of elastomers that consist of magnetic components [e.g., carbonyl iron powder (CIP)] and nonmagnetic materials that have a low elastic modulus (e.g., similar to that of polyurethane or rubber) (*44*–*46*). Because an MRE, due to its magnetic components, has higher relative permeability (=5 to 7) than that of nonmagnetic materials such as polyurethane or rubber (=1), it can be used as a footpad with a lower reduction of holding force in the normal direction (*47*). However, because the relative permeability of an MRE is still lower than that of pure iron (=4000), a thicker MRE design can decrease normal holding force up to the amount that can result in the decrease of shear holding force even with the large coefficient of friction (*48*). On the contrary, if the structure is too thin, then it can easily tear.

Using the magnetic circuit analysis, we determined an acceptable thickness range for the MRE that does not lead to decreases in holding force in the shear direction compared with S-EPMs without MREs. As shown in Fig. 4E, on the basis of the measured coefficient of friction in fig. S1, we found that an MRE footpad with a thickness of less than 0.75 mm has a larger shear holding force compared with an S-EPM without an MRE footpad. In this study, a 0.25-mm-thick MRE was manufactured; it is thin enough to satisfy the thickness requirements and, at the same time, did not tear easily. The detailed manufacturing process is provided in Materials and Methods. The designed S-EPM with the MRE footpad weighed 169 g. With a 0.25-mm-thick MRE, the holding forces in the normal direction and the shear direction were measured to be 535.4 and 444.6 N (averaged from five trials), respectively. Without the MRE, the holding forces in the normal direction and shear direction were measured to be 697.1 and 129.3 N (averaged from five trials), respectively (table S1).

Low-height, three-DOFs compliant passive ankle

A simple and lightweight ankle design was proposed that enabled the foot to attach to the substrate robustly. Because the height of the ankle joint to the contact surface acts as a moment arm during climbing vertical walls, the height should be low to prevent large moments that can cause tipping over of the foot from the surface. Considering this requirement, we designed a three-DOFs passive, compliant ankle with a 13-mm height from the pole surface (Fig. 3A). Due to the squared geometry of the S-EPM, we were able to place the ankle joint inside the center of the S-EPM, enabling low-height ankle and compact foot design. The ankle height was chosen to be 13 mm, considering sufficient operation ranges of the legs for locomotion tasks, because too-low ankle height can cause interference between the leg link and the S-EPM.

The ankle consists of a stainless steel ball joint and two rubber bands. This ball joint transmits only forces to the ankle, and the rubber band's compliance enables robust foot attachment. The designed ankle allows leg rotation in the pitch direction from 0° to +90°, roll direction from −6° to +6°, and yaw direction from −11° to +11°; the rotations in the roll and yaw directions were more restricted compared with pitch direction so that the ball joint could be firmly mounted. With this large pitch angle range, the robot can move in fore-aft directions at a fast speed. Parts for mounting the ankle and the rubber band were 3D printed for lightweight design; however, for a larger payload, the mounting materials could be replaced with stiff and nonferromagnetic materials such as aluminum or stainless steel.

Foot design and the region of admissible reaction forces

The foot design consisting of the S-EPM and MRE footpad enabled large normal and shear holding forces, whereas the ankle joint designed to be closely located to the contact surface reduced foot-tipping moments during locomotion. These foot design features allowed the robot to apply large forces to the environments without detaching, slipping, or tipping over of the foot. We quantified these forces that the robot can apply to the environments while maintaining stable foot attachments by considering reaction forces at the ankle joint. Figure 4F shows the region of admissible reaction forces at the ankle joint, which is defined by the set of ankle reaction forces, denoted by $\mathbf{f}_A$, that prevent the foot from slipping or tipping over. The region of admissible $\mathbf{f}_A$ is represented by the overlapped region under the two cones. The region below the cone with a dashed line represents conditions avoiding the foot slipping, and the region below the cone with a solid line represents conditions avoiding the foot tipping over. A detailed derivation is presented in Materials and Methods. Considering the maximum joint torques at each leg, MARVEL can only produce an ankle reaction force $\mathbf{f}_A$ value lower than 250 N in the normal direction at nominal leg configurations. Therefore, we only consider the region under the horizontal line of 250 N, as shown in Fig. 4F.

In the derivation of the region of admissible $\mathbf{f}_A$, the normal holding force determines the vertical position of the vertex of the two cones, whereas the coefficient of friction and the height of the ankle joint determine the slope of the two cones. Therefore, large magnetic holding forces of the S-EPM, large coefficients of friction due to the MRE footpad, and the low ankle joint height will enable a large region of admissible $\mathbf{f}_A$. Although adding the MRE footpad decreases the magnetic holding force of the S-EPM, it increases the coefficient of friction. Overall, as shown in Fig. 4F, the region of admissible $\mathbf{f}_A$ of the foot design with the MRE footpad (blue area) is larger than that of the foot design without the MRE footpad (red area). This implies that instead of increasing the holding force in the normal direction, which would force us to increase the weight of the magnetic foot, we can broaden the region of admissible $\mathbf{f}_A$ by integrating the S-EPM and MRE footpad. As a result, the magnetic foot with the wide region of admissible $\mathbf{f}_A$ can support large shear (traction) forces required for dynamic climbing locomotion. This region of admissible $\mathbf{f}_A$ will vary according to the magnetic holding force, which can be reduced by gaps caused by surface conditions. Therefore, the region of admissible

$\mathbf{f}_A$ for the surface condition should be calculated with the magnetic holding forces at different air gaps.

In summary, synergistic integration of the EPM and MRE enabled the magnetic foot to produce large holding forces in normal and shear directions. Especially, the proposed S-EPM geometry with improved switching performance could ensure instantaneous adhesion switching, an untethered robot system with onboard power, and a low-height ankle design. Last, using the passive compliant ankle, the foot could even adapt to curved steel substrates compliantly and without slipping or tipping over, as shown in the experiments conducted on the curved surface of the storage tank.

Locomotion control framework

MARVEL's modes of locomotion include floors, vertical surfaces, and inverted surfaces; all modes use the same control framework. As shown in Fig. 5A, the controller consists of three submodules: a motion plan module used to provide desired robot behaviors, a stance motion control module to track the desired body configuration, and a swing motion control module for foot placement and to manage attachment and detachment of the magnetic feet.

Motion plan

The purpose of the controller is to provide a set of control signals to realize the desired robot behavior. Such behavior can be concisely represented by a set of numeric commands with physical equivalents. The commands provided by the motion plan module include the desired robot state and a contact schedule that defines a gait or a sequence of contact states over time. Each foot has four contact states, namely, the swing phase and stance phases with floor, wall, and ceiling. In our framework, these commands can be provided by a motion library or a human operator using a joystick. A motion library comprises a number of predefined desired motions over time, and it can be generated by a high-level motion planning algorithm (sampling-based optimization and trajectory optimization) or manually designed by a human operator.

Stance motion control

The stance motion control module attempts to find the appropriate force distribution of the supporting legs to track the desired body motions. However, controlling the robot's dynamic motion is a nontrivial task because the equation of motion is highly nonlinear, and the robot body is underactuated; it can only be indirectly controlled by the internal interaction forces, along with external forces acting on the feet via contact interactions in the environment while the robot attempts to respect constraints such as actuator limitations and contact constraints. Recently, the model predictive control (MPC) approach has proven successful at solving this kind of problem (*49*–*53*).

Because our robot aims to demonstrate complex climbing maneuvers in 3D space, we adopted a nonlinear MPC (NMPC) approach proposed in (*54*), free from the issues related to Euler angles and quaternion as an orientation representation. This approach relies on the use of simplified dynamics, namely, the single rigid body dynamics shown in Fig. 5B, to predict the robot's future behavior and determine the optimal distribution of GRFs at the supporting feet to achieve the desired body motions. Although single rigid body dynamics does not represent the full complexity of the system, it provides tractable model accuracy and computational efficiency under the assumption that leg dynamics is negligible (*50*–*53*). For MARVEL, this assumption is reasonable because the leg mass (0.3355 kg without the magnetic foot) is negligible compared with the total robot mass (8 kg).

For stable attachment of the foot to the surfaces, the ankle reaction forces $\mathbf{f}_A$ in the stance phases should be chosen to stay within the region of admissible $\mathbf{f}_A$. By explicitly incorporating these constraints into the NMPC formulation, the controller enables the robot to robustly traverse both vertical and inverted surfaces without slipping or the foot tipping over.

Swing motion control

Desired motions of the swing legs were considered independently for each leg and were generated using a cubic Bézier curve that interpolates the two ends of each foot position. The estimated foothold position at liftoff, the desired foot height above the substrate, and the desired landing foothold position represented in the inertial frame were used to generate the foot reference. The desired landing foothold position was calculated in a way similar to Raibert's heuristic method, introduced in (*55*). Given the desired position and velocity of each foot, the joint torques to track these references can be generated using the task-space proportional derivative controller with the virtual model control approach (*56*).

To safely attach and detach feet and implement climbing locomotion, the switching time and the air gap at the time instant of EPM magnetization should be appropriately considered in the swing phase. Discrete time intervals (5 ms) to switch the state of the EPM were inserted at the beginning and end of the swing phase. The desired foothold position at the end of the swing phase was modified such that the foot penetrated slightly below the substrate surface, generating the correct amount of pressure on the foot to reduce the air gap between the EPM and the substrate.

Agile locomotion on vertical and inverted surfaces

This section presents experimental results that demonstrate MARVEL's agile locomotion capabilities, including crawl, pace, and trot gait, which together enable forward and backward movement as well as turning movements on vertical and inverted surfaces. In these experiments, MARVEL's desired motions were commanded via a joystick by a human operator. Commands include heading and lateral linear velocities and yaw rate expressed in the body frame. The desired body positions can be obtained simply by integrating the desired velocities with respect to time; the remaining desired states were set to zero, except that the desired body height was set to 0.15 m above the substrate because a body height lower than this value could cause collisions of the leg links with the substrate.

First, the climbing skills of MARVEL on a vertical wall, including crawl (i.e., only one leg in the swing phase at a time) and pace gait (i.e., left pair and right pair of legs alternating), were demonstrated. The robot was commanded to use crawl gait and increase its heading velocity to 0.35 m/s; it then set the velocity to zero after reaching the end of the wall. The resulting motion is shown in movie S1. Another experiment was carried out to show MARVEL's turning ability on a vertical wall; results showing the robot following a curved trajectory can be seen in Fig. 1A and movie S1.

In addition to crawl gait, pace gait was used to evaluate MARVEL's agile climbing capability. The resulting motion is shown in movie S2. As shown in Fig. 6Ai, MARVEL was able to reach a maximum average speed of around 0.7 m/s (2.12 body lengths/s), which is comparable with the speed of a gecko (0.77

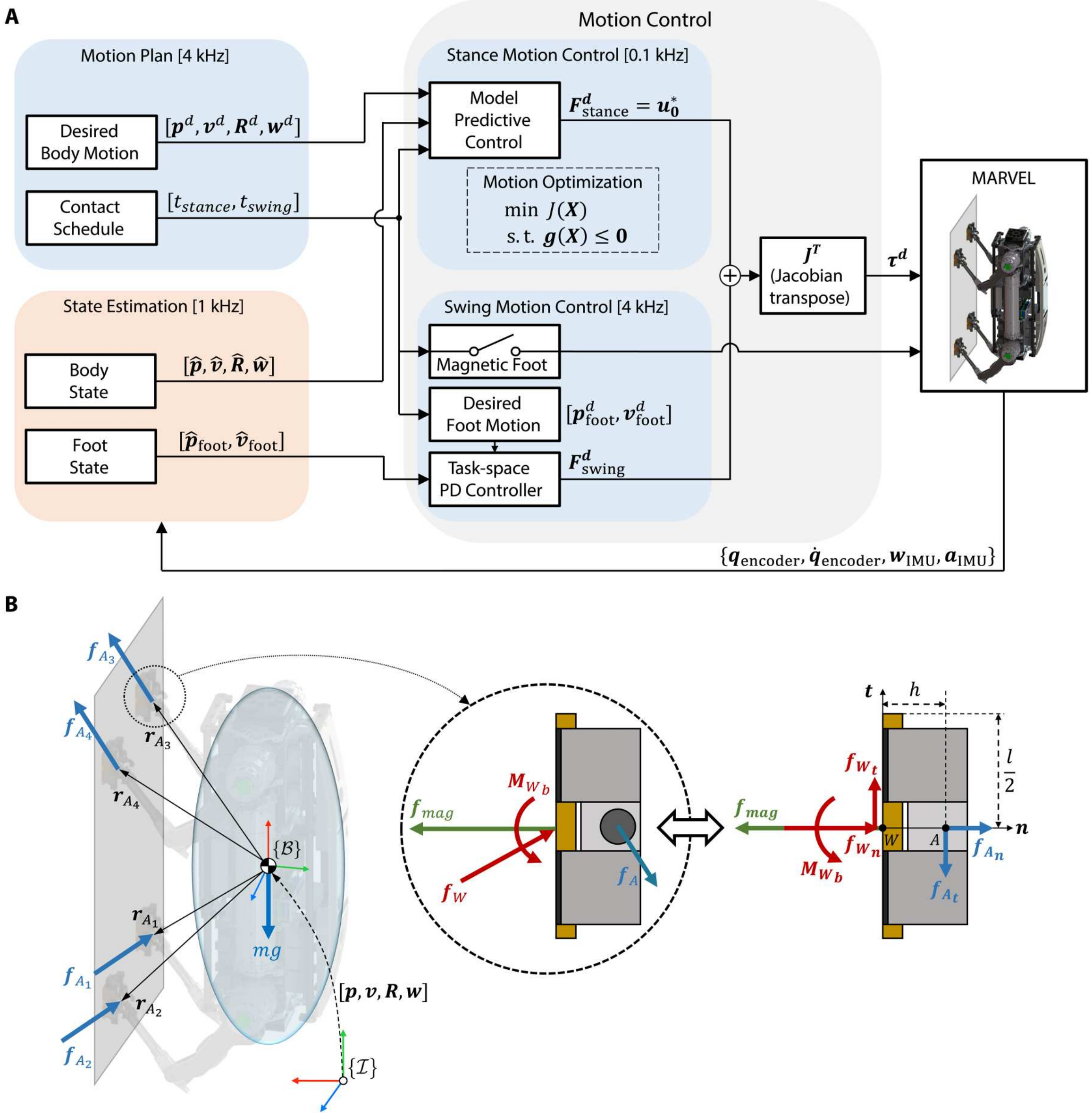

Fig. 5. Locomotion control architecture and the dynamics model of MARVEL. (**A**) Overall control architecture. (**B**) The entire rigid body dynamics is approximated as single rigid body dynamics. [$\mathbf{p}$, $\mathbf{v}$, $\mathbf{R}$, $\mathbf{w}$] ∈ [$\mathbb{R}^3$, $\mathbb{R}^3$, SO(3), $\mathbb{R}^3$] are the position, velocity, orientation, and angular velocity, respectively, of the robot body with respect to the inertia frame $\mathcal{I}$; m is the total robot mass; $\mathbf{g} \in \mathbb{R}^3$ is the gravitational acceleration; $\mathbf{f}_{A_i} \in \mathbb{R}^3$ is the ankle reaction force exerted on the ith ankle joint; and $\mathbf{r}_i \in \mathbb{R}^3$ is the vector from the robot body to the ith ankle joint. The zoomed-in view shows the free-body diagram of the magnetic foot when it statically adhered to vertical surfaces.

m/s) as reported in (*38*). Figure 6A (ii and iii) shows the estimated $\mathbf{f}_A$ applied at each foot in the sagittal plane. The estimated $\mathbf{f}_A$ can be obtained using the current sensor and encoder sensor data of motors at each leg, the current-torque relationship of the motors, and the kinematics of each leg. We found that the estimated $\mathbf{f}_A$ in both tangential and normal directions peaked when MARVEL reached the maximum speed. It was also observed that the estimated $\mathbf{f}_A$ stayed within the region of admissible $\mathbf{f}_A$ during experiments, as shown in Fig. 6Aiv.

We next show MARVEL's locomotion capabilities on an inverted surface. The robot was commanded to use a trot gait (i.e., diagonal pairs of legs alternating) and to increase its heading velocity to 0.5 m/s. The resulting motion is shown in movie S3. Figure 6B shows the heading velocity and estimated $\mathbf{f}_A$ applied at each foot in the sagittal plane during the experiment. MARVEL can stably track the desired commands and move at speeds of up to 0.5 m/s (1.51 body lengths/s). MARVEL's turning mobility on inverted surfaces is depicted in Fig. 1B and movie S3, in which MARVEL was commanded to follow a circular path with a radius of 0.4 m.

Versatile locomotion on vertical and inverted surfaces

This section presents various experimental results to show MARVEL's versatile locomotion ability in different climbing scenarios. These scenarios include stepping over a 10-cm-wide gap,

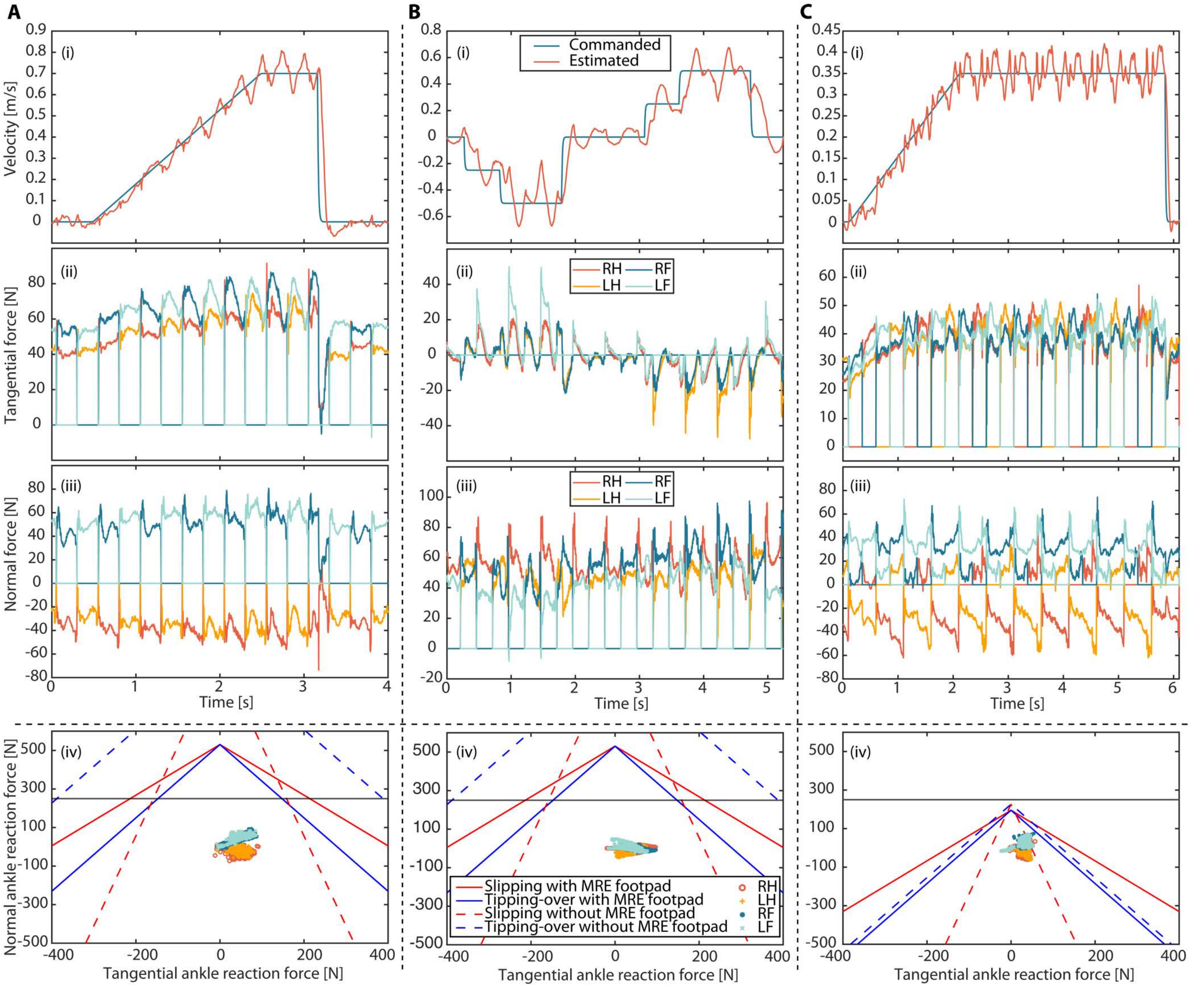

Fig. 6. Experimental data of agile locomotion tasks. (**A**) Pacing on a vertical surface. (**B**) Trotting on an inverted surface. (**C**) Crawling on a locally curved storage tank. RH, RF, LH, and LF indicate right hind leg, right fore leg, left hind leg, and left fore leg, respectively.

overcoming a 5-cm-high obstacle, and performing transitions from floor to wall and from wall to ceiling.

For the gap-crossing and obstacle-overcoming experiments, handcrafted motions stored in the motion library were provided to the robot. Both motions start and end with a nominal standing pose, with all feet in contact with the wall. For the gap-crossing motion, the robot was guided to move in the heading direction; then, each foot was sequentially placed across the gap while keeping the other three feet on the wall. The obstacle-overcoming motion was similar to the gap-crossing motion, but the pitch rotation of the body was added to attain kinematic workspace of the feet for obstacle clearance. The resulting motions are shown in Fig. 1C and movie S4.

The transition experiment began with the robot standing in front of a corner until a human operator initiated the transition. Having placed two front feet on the wall, MARVEL set the desired body pitch rate to a constant value until the body pitch angle reached a vertical upright pose. In the meantime, the distance between the front (hind) end of the robot body and the wall (floor) in the *x* direction (*z* direction) was regularized to a given value by modifying the desired body velocity in the *x* direction (*z* direction). The floor-to-wall transition was then terminated by placing the two hind feet on the wall. The wall-to-ceiling transition could be accomplished using a similar procedure to the floor-to-wall transition. The resulting motions are shown in Fig. 1D and movie S5.

Real-world applications

Because of the accumulation of paint, dust, and rust, surface conditions of real-world steel structures are rough. As a demonstration of MARVEL's potential applications in the real world, we performed outdoor experiments, including forward, backward, and turning movement, as well as obstacle-overcoming experiments on a storage tank made of steel, a vertical cylindrical shape with a diameter of 3 m (movie S6). The surface of the tank was covered with up to 0.3-mm-thick paint, and as shown in the zoomed-in view of Fig. 1E, the painted surface was covered with rust and dust. In addition, because of the curvature of the tank, there was an additional air gap of up to 0.143 mm at the edge of the footpad. This increased air gap will decrease the magnetic holding force f_{mag}, eventually reducing the region of admissible $\mathbf{f}_A$. Although the surface of the storage tank was rough and curved, MARVEL was able to successfully traverse it by allowing the passive ankle joints to compliantly adjust to the curved surface; furthermore, the magnetic feet provided sufficient holding force without slipping or tipping over (Fig. 1E). The maximum achieved speed was 0.35 m/s with crawling gait, as shown in Fig. 6Ci. Figure 6Civ shows the estimated $\mathbf{f}_A$ along with the region of admissible $\mathbf{f}_A$ of the foot design with and without MRE footpads during the crawl gait. We observed that the estimated $\mathbf{f}_A$ stayed within the region of admissible $\mathbf{f}_A$ in the case of the MRE footpads, but it went beyond the region of admissible $\mathbf{f}_A$ in the case without MRE footpads. These results demonstrate that the unconventional foot design integrated with the S-EPM and MRE footpads provides sufficient traction forces for dynamic vertical climbing motions.

Payload capability

We investigated the payload capacity of MARVEL on both vertical and inverted surfaces. During the experiments, the weight of the payload was not informed to the controller. Although the payloads acted as disturbances to the system, MARVEL was able to carry them up to 2 kg (0.25 body weight) and 3 kg (0.375 body weight) on vertical and inverted surfaces, respectively, while moving at the speed of 0.1 m/s (Fig. 1F and movie S7).

DISCUSSION

Legged robots have achieved substantial progress and can now perform highly dynamic and versatile locomotion over a broad range of unstructured terrains. This work enables such locomotion on vertical and inverted walls, thereby enlarging the operational workspace of legged robots. To enable dynamic and versatile climbing locomotion, we present a synergistic combination of the following design components: S-EPMs, which can generate and eliminate magnetic adhesion instantaneously with low energy consumption; MRE footpads that provide larger shear holding force, sacrificing only a small amount of normal holding force; and proprioceptive actuators with a reliable controller that allows the robot to dynamically move in 3D space without the foot slipping or tipping over. With a combination of the S-EPM and MRE, we were able to develop a magnetic foot that has sufficient holding force in both normal and shear directions. In addition, because of the special geometry of the S-EPM, the low-height passive compliant ankle can be compactly integrated with legs driven by proprioceptive actuators. Last, proprioceptive actuators and control design enable the robot to exert a force that does not induce failures such as the foot slipping or tipping over.

Table 1 compares MARVEL with other climbing legged robots in terms of adhesion mechanism, body mass and length, the number of legs and actuators, maximum locomotion speed, executable locomotion tasks and gaits, and maximum payload. MARVEL excels over other climbing robots in terms of climbing speed and ability to execute various motions. It demonstrates the fastest vertical and inverted walking speed, whereas its versatile locomotion ability enables the highest number of gaits and locomotion tasks. Previous robots (*17*–*19*) achieved high speed (locomotion) at the cost of degraded maneuverability because of the limited number of actuators. Another family of climbing legged robots (*1*, *24*, *25*, *27*–*29*), which have fully actuated leg structures, is equipped with high gear ratio transmissions to maximize the actuator's torque density. Despite their wide range of maneuverability, the benefits come at the cost of low output speed and low-bandwidth torque control capability, which are not suitable for high-speed locomotion. For robots using EPMs, the slow switching time of the holding force of the EPM also limits the climbing speed (*28*, *29*). Compared with these robots, MARVEL's enhanced agility with versatile climbing ability is the result of the design of a developed fast-switching strong magnetic foot combined with actuation and control schemes adopted from dynamic quadrupedal robots. The magnetic foot design combines S-EPMs with the MRE footpads, enabling fast switching and strong holding force in the normal and shear directions. This magnetic foot is compared with other types of adhesion mechanisms in table S2.

MARVEL's potential application is to investigate industrial sites, such as steel-structured buildings, bridges, ships, or storage tanks. These sites inevitably involve tasks at high altitudes or confined spaces, such as the inspection of steel bridges or shipyard welding platforms, which could be dangerous for human workers (*57*, *58*). As a real-world demonstration on industrial environments, MARVEL's locomotion capability was tested on a storage tank. Although the storage tank surface was curved and covered with dust and paint, MARVEL was able to climb on the surface at a speed up to 0.35 m/s while avoiding collision with protrusions and overcoming obstacles. However, after conducting the set of experiments on rough surfaces (the experiments shown in supplementary movies and multiple other trials that were not recorded), we found that small edge parts of the MRE footpads were separated from enveloping PMC-770. This separation could be due to weak connections between two different soft materials, the MRE footpads and PMC-770.

Although our approach allows for dynamic and versatile locomotion in real-world scenarios, several opportunities exist for design component upgrades. Because of the flat-pole surface of the S-EPM, the proposed magnetic foot has limited adhesion on very irregular or sharply curved surfaces. To overcome this limitation, a compliantly integrated multiple miniaturized EPM with the MRE footpad can adapt to surfaces with roughness and curvature, increasing effective contact area and adhesion. We can also improve actuator schemes and controllers for better locomotion performance. So far, we have used a proprioceptive actuator design optimized for dynamic jumping at ground level; however, a leg and actuator design optimized for dynamic climbing motion will be more effective for climbing robots. The reference trajectory that we implemented was mainly based on handcrafted heuristic tuning; however, using a vision sensor, motion planner, and trajectory optimization, MARVEL will be able to climb and perform various tasks autonomously.

MATERIALS AND METHODS

MRE footpad fabrication

The process of MRE fabrication is illustrated in Fig. 7A. As a compliant material, we used PMC-770 polyurethane rubber produced

Table 1. Comparison of climbing legged robots. BL, body length; N/A, not available. 90° and 180° refer to vertical and inverted directions.

Climbing robot	Adhesion method	Mass (kg)	Num. of legs/ actuators	BL (mm)	Max. speed (cm/s) (BL/s)	Versatile locomotion capability	Max. payload (kg) (payload-to-weight ratio)	Gait pattern
MARVEL (untethered)	Electropermanent magnetic	8	4/12	330	90°: 70 (2.12) 180°: 50 (1.51)	Forward walk, lateral walk, turning, gap crossing, obstacle overcoming, and transition	90°: 2 (0.25) 180°: 3 (0.375)	Crawl gait, Trot gait, Pace gait
NINJA-1 (*1*) (tethered)	Pneumatic	45	4/12	1800	90°: 2 (0.0111) 180°: 5 (0.0278)	Forward walk and lateral walk	N/A	Wall gait
ROMA II (*3*) (tethered)	Pneumatic	25	2/5	555	90°: 2.5 (0.045)	Forward walk	90°: 5 (0.2)	Bipedal gait
Stickybot (*11*) (untethered)	Dry adhesion	0.37	4/12	600	90°: 4 (0.07)	Forward walk	N/A	Trot gait
SpinybotII (*13*) (untethered)	Spine	0.4	6/7	580	90°: 2.3 (0.04)	Forward walk	90°: 0.4 (1.0)	Tripod gait
RiSE V3 (*17*) (untethered)	Claw	5.4	4/9	700	90°: 21 (0.3)	Forward walk	N/A	Crawl-bound
CLASH (*18*) (untethered)	Spine	0.015	6/1	100	90°: 15 (1.5)	Forward walk	N/A	Tripod gait
DynoClimber (*19*) (untethered)	Claw	2.6	2/2	400	90°: 67 (1.675)	Forward walk	N/A	Bipedal gait
HAMR-E (*20*) (tethered)	Electroadhesion	0.00148	4/8	45	90°: 0.12 (0.026) 180°: 0.45 (0.1)	Forward walk, lateral walk, and turning	N/A	Crawl gait
ASTERISK (*24*) (tethered)	Permanent magnet	1.5	6/24	816	180°: 0.3 (0.0037)	Forward walk and lateral walk	N/A	Square gait
REST 1 (*25*) (untethered)	Electromagnet	220	6/18	1100	N/A	Forward walk and lateral walk	90°: 100 (0.45) 180°: 100 (0.45)	Tripod gait
Magneto (*28*) (tethered)	Electropermanent magnet	5.87	4/12	370	90°: 1.5 (0.04) 180°: 1.5 (0.04)	Forward walk, lateral walk, turning, and gap crossing	90°: 1.5 (0.25)	Crawl gait

by Smooth-On Inc. because of its excellent friction and wear performance. As magnetic particles, CC-grade CIP from BASF (Badische Anilin und Soda Fabrik) was used for its high magnetic permeability, high saturation magnetization, and low residual induction of the MRE (*46*, *59*).

The fabrication method of the MRE membrane was taken from (*60*). First, we prepared a flat plate with two parallel edges of 0.25-mm tape strips, of which thickness is equal to that of the MRE footpad (Fig. 7A, 1). After that, PMC-770 was mixed with CIP at a volume ratio of 4 to 6 (Fig. 7A, 2). To prevent the agglomeration of powder, we filtered the powder through a fine-mesh sieve, poured it into the PMC-770 several times (Fig. 7A, 3), and then mixed the magnetorheological mixture using a hand drill (Fig. 7A, 4). Air bubbles in the mixture were removed by a vacuum defoamer (Fig. 7A, 5). The mixture was poured onto the flat plate (Fig. 7A, 6). Then, a flat bar was pushed along the tape in one direction to spread the mixture (Fig. 7A, 7). After curing time (about 12 hours) at room temperature, we gently removed the thin MRE membrane from the plate (Fig. 7A, 8).

Magnetic foot manufacturing

The manufacturing process of the S-EPM started with an attachment of AlNiCo magnets to keepers. AlNiCo magnets were inserted into the square-shaped holes of the keepers, and Loctite 401 was thinly applied to the boundaries between AlNiCo magnets and keepers. We then wound an enamel wire around the AlNiCo magnets to make coils. To prevent the coil from unwinding at both ends, coil barriers were 3D printed and attached to the keepers using Loctite 401. After winding coils, we attached NdFeB magnets to the keepers in the same manner used for the AlNiCo magnets.

The integration of the S-EPM and MRE footpad was as follows: MRE footpads were cut from the MRE membrane and attached to individual poles of keepers (Fig. 7B, 1). To firmly integrate the S-

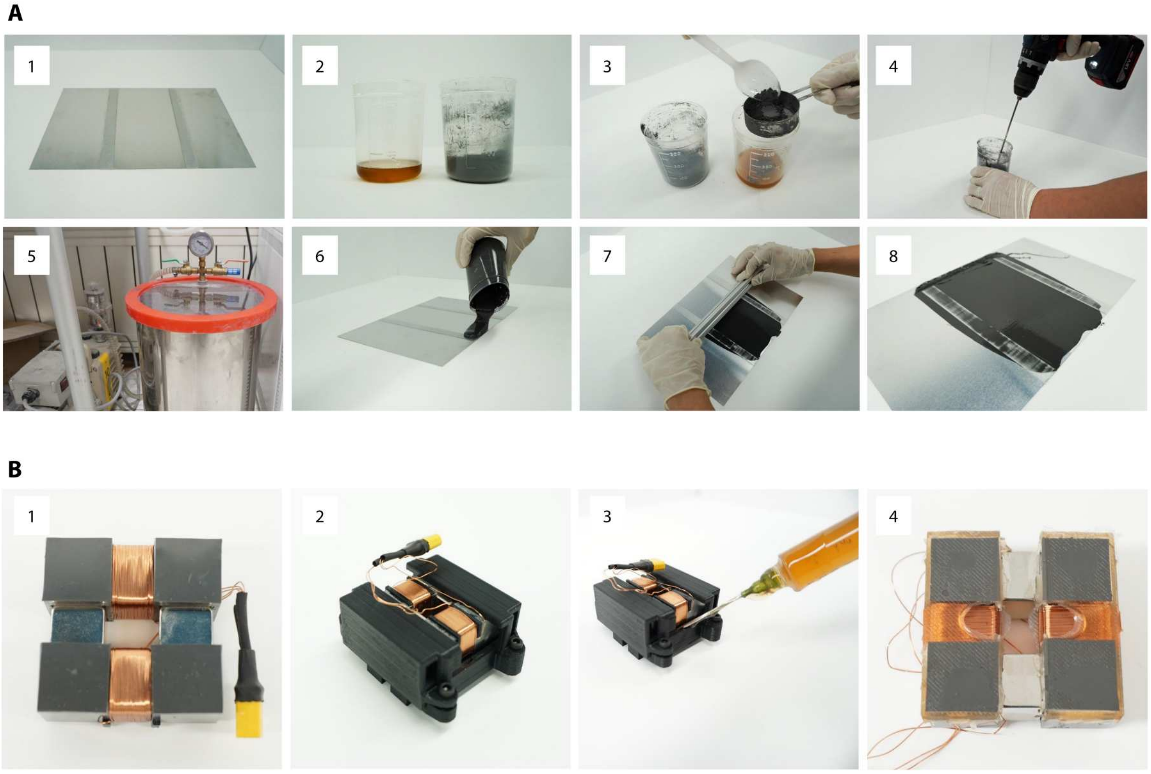

Fig. 7. MRE fabrication and integration of the S-EPM and MRE. (**A**) Fabrication process of MRE membranes. (**B**) Integration process of S-EPM and MRE footpad. Using a 3D printed mold, we sealed the S-EPM and MRE footpad with PMC-770.

EPM and the MRE footpads, we sealed them using PMC-770. The sealing process consisted of putting the S-EPM and the MRE footpads into 3D printed molds and pressing the S-EPM to prevent PMC-770 from permeating under the MRE pads (Fig. 7B, 2). PMC-770 was poured using a syringe (Fig. 7B, 3). After curing time (about 12 hours) at room temperature, we disassembled the integrated S-EPM and MRE footpads from the molds (Fig. 7B, 4).

Region of admissible ankle reaction forces

This section provides the derivation of the region of admissible reaction forces that ensures that the magnetic feet are firmly attached to the substrate without tipping over or slipping. Considering the free-body diagram provided in Fig. 5B, the weight of the magnetic foot can be neglected because its magnitude is negligible compared with the other forces. When the velocity and acceleration of the magnetic foot are zero, we can obtain, via static equilibrium, the GRF $\mathbf{f}_W$ and the bending moment $\mathbf{M}_W$ at point W

$$\begin{aligned} f_{W_n} &= f_{\text{mag}} - f_{A_n} \\ f_{W_t} &= f_{A_t},\ f_{W_b} = f_{A_b} \\ M_{W_b} &= h\, f_{A_t},\ M_{W_t} = h\, f_{A_b} \end{aligned} \tag{1}$$

where the subscript represents each component of the right-handed Cartesian coordinate frame ($\mathbf{n}$, $\mathbf{t}$, $\mathbf{b}$) that consists of the normal, tangential, and binormal directions with respect to the contact surface; f_{mag} is the magnetic force; $\mathbf{f}_A$ is the ankle reaction force applied by the ankle joint onto the robot at point A; and h is the ankle height. According to the Coulomb friction model, the magnetic foot will remain attached without slipping as long as the GRF $\mathbf{f}_W$ lies within the friction cone

$$f_{W_n} \geq 0,\ \sqrt{f_{W_t}^2 + f_{W_b}^2} \leq \mu_s f_{W_n} \tag{2}$$

where μ_s is the coefficient of friction. Alternatively, the friction cone can be represented in terms of the $\mathbf{f}_A$ by substituting Eq. 1 into Eq. 2 as

$$\mathcal{C} = \left\{ \mathbf{f}_A \mid f_{A_n} \leq f_{\text{mag}},\ \sqrt{f_{A_t}^2 + f_{A_b}^2} \leq \mu_s \left(f_{\text{mag}} - f_{A_n} \right) \right\} \tag{3}$$

For computational purposes, a friction pyramid $\mathcal{P}$ (i.e., four-sided polyhedral cone) can be used to approximate the friction cone $\mathcal{C}$

$$\begin{aligned} \mathcal{P} = \Big\{ \mathbf{f}_A \mid f_{A_n} \leq f_{\text{mag}},\ | f_{A_t} | \leq \mu_s \left(f_{\text{mag}} - f_{A_n} \right),\ | f_{A_b} | \\ \leq \mu_s \left(f_{\text{mag}} - f_{A_n} \right) \Big\} \end{aligned} \tag{4}$$

Whereas slipping failure is closely related to shear or tangential force, the other mode of failure, the foot tipping over, is mainly related to the bending moment. In the derivation process, the footpad material (MRE) is assumed to have homogeneous and linear elastic properties; therefore, the normal stress will change linearly over the contact area. Because of the symmetry of the magnetic foot, the normal stress $\sigma_{\mathbf{b}}$ induced by the bending moment $\mathbf{M}_{W_\mathbf{b}}$ at any distance t from point W can be calculated according to the flexure formula (*61*)

$$\sigma_b(t) = -\frac{M_{W_b}}{I} t \tag{5}$$

where I is the moment of inertia of the contact area about the binormal axis **b** at point W, and the distribution of $\sigma_{\mathbf{b}}(t)$ is shown in fig. S2A. The normal stress distribution induced by the normal force $\mathbf{f}_{W_\mathbf{n}}$, shown in fig. S2B, can be obtained by

$$\sigma_n = \frac{f_{W_n}}{A} \tag{6}$$

where A is the contact area. Via the principle of superposition, the resultant normal stress distribution, shown in fig. S2C, can be determined as

$$\sigma(t) = \sigma_b(t) + \sigma_n = -\frac{M_{W_b}}{I} t + \frac{f_{W_n}}{A} \tag{7}$$

The minimum normal stress occurs at the top of the contact area

$$\begin{aligned} \sigma_{\min} &= \sigma_b(l/2) + \sigma_n \\ &= -\frac{6h}{l^3} f_{A_t} + \frac{1}{l^2}\left(f_{\text{mag}} - f_{A_n}\right) \end{aligned} \tag{8}$$

To prevent magnetic foot detachment from the substrate, the minimum normal stress $\sigma_{\min}$ must be nonnegative, which results in the following

$$f_{A_n} \le f_{\text{mag}},\ f_{A_t} \le \frac{l}{6h}\left(f_{\text{mag}} - f_{A_n}\right) \tag{9}$$

Applying a similar procedure to the case in which the bending moment is in the opposite direction and the cases in the (**b**, **n**) plane, we can obtain a four-sided polyhedral cone $\mathscr{B}$ formed by a set of inequality constraints, as in

$$\mathcal{B} = \left\{ f_A \mid f_{A_n} \le f_{\text{mag}}, \mid f_{A_t} \mid \le \mu_t\left(f_{\text{mag}} - f_{A_n}\right), \mid f_{A_b} \mid \le \mu_t\left(f_{\text{mag}} - f_{A_n}\right) \right\} \tag{10}$$

where $\mu_t := l/(6h)$ defines the coefficient of tipping over. Therefore, the magnetic foot will remain attached without the foot tipping over as long as the $\mathbf{f}_A$ lies within the four-sided polyhedral cone $\mathscr{B}$.

In conclusion, to ensure that the magnetic foot firmly attaches to the substrate, the $\mathbf{f}_A$ should lie within the admissible region, which is the intersection of sets spanned by the inequalities in Eqs. 3 and 10, as shown in fig. S2D. Intuitively, if μ_t is smaller than μ_s, then any $\mathbf{f}_A$ out of the admissible region would initiate tipping over of the magnetic foot from the substrate before slip occurs (fig. S2E); in contrast, if μ_t is larger than μ_s, then any $\mathbf{f}_A$ out of the admissible region would cause a slip motion before detachment caused by tipping over (fig. S2F). Therefore, to enlarge the admissible region, it is important to increase the coefficient of friction μ_s of the magnetic foot and to increase the coefficient of tipping over μ_t by reducing the height of the ankle. This admissible region is explicitly considered to produce appropriate ankle reaction forces in the control design.

Supplementary Materials

This PDF file includes:
Sections S1 to S6
Figs. S1 to S6
Tables S1 to S5
Reference (*62*)

Other Supplementary Material for this manuscript includes the following:
Movies S1 to S7

REFERENCES AND NOTES

1. S. Hirose, A. Nagakubo, R. Toyama, Machine that can walk and climb on floors, walls and ceilings, in *Fifth International Conference on Advanced Robotics Robots in Unstructured Environments* (IEEE, 1991), pp. 753–758.
2. M. Minor, H. Dulimarta, G. Danghi, R. Mukherjee, R. L. Tummala, D. Aslam, Design, implementation, and evaluation of an under-actuated miniature biped climbing robot, in *IEEE/RSJ International Conference on Intelligent Robots and Systems* (IEEE, 2000), vol. 3, pp. 1999–2005.
3. C. Balaguer, A. Gimenez, A. Jardón, Climbing robots' mobility for inspection and maintenance of 3D complex environments. *Auton. Robot.* **18**, 157–169 (2005).
4. W. Brockmann, Concept for energy-autarkic, autonomous climbing robots, in *Climbing and Walking Robots* (Springer, 2006), pp. 107–114.
5. C. Balaguer, A. Giménez, J. M. Pastor, V. Padron, M. Abderrahim, A climbing autonomous robot for inspection applications in 3d complex environments. *Robotica* **18**, 287–297 (2000).
6. M. Tavakoli, A. Marjovi, L. Marques, A. T. de Almeida, 3Dclimber: A climbing robot for inspection of 3D human made structures, in *IEEE/RSJ International Conference on Intelligent Robots and Systems* (IEEE, 2008), pp. 4130–4135.
7. A. Parness, N. Abcouwer, C. Fuller, N. Wiltsie, J. Nash, B. Kennedy, Lemur 3: A limbed climbing robot for extreme terrain mobility in space, in *IEEE International Conference on Robotics and Automation* (IEEE, 2017), pp. 5467–5473.
8. D. Bevly, S. Dubowsky, C. Mavroidis, A simplified cartesian-computed torque controller for highly geared systems and its application to an experimental climbing robot. *J. Dyn. Syst. Measurement Control* **122**, 27–32 (2000).
9. T. Bretl, Motion planning of multi-limbed robots subject to equilibrium constraints: The free-climbing robot problem. *Int. J. Rob. Res.* **25**, 317–342 (2006).
10. B. Kennedy, A. OkonLemur, H. Aghazarian, M. Badescu, X. Bao, Y. Bar-Cohen, Z. Chang, B. E. Dabiri, M. Garrett, L. Magnone, S. Sherrit, Lemur IIb: A robotic system for steep terrain access. *Industrial Robot.* **33**, 265–269 (2006).
11. S. Kim, M. Spenko, S. Trujillo, B. Heyneman, D. Santos, M. R. Cutkosky, Smooth vertical surface climbing with directional adhesion. *IEEE Transact. Robot.* **24**, 65–74 (2008).
12. S. Kim, A. T. Asbeck, M. R. Cutkosky, W. R. Provancher, SpinybotII: Climbing hard walls with compliant microspines, in *12th International Conference on Advanced Robotics* (IEEE, 2005), pp. 601–606.
13. A. T. Asbeck, S. Kim, M. R. Cutkosky, W. R. Provancher, M. Lanzetta, Scaling hard vertical surfaces with compliant microspine arrays. *Int. J. Robot. Res.* **25**, 1165–1179 (2006).
14. K. Autumn, M. Buehler, M. Cutkosky, R. Fearing, R. J. Full, D. Goldman, R. Groff, W. Provancher, A. A. Rizzi, U. Saranli, A. Saunders, D. Koditschek, Robotics in scansorial environments, in *Unmanned Ground Vehicle Technology VII* (SPIE, 2005), vol. 5804, pp. 291–302.
15. A. Saunders, D. I. Goldman, R. J. Full, M. Buehler, The rise climbing robot: Body and leg design, in *Unmanned Systems Technology VIII* (SPIE, 2006), vol. 6230, pp. 401–413.
16. M. Spenko, G. C. Haynes, J. A. Saunders, M. R. Cutkosky, A. A. Rizzi, R. J. Full, D. E. Koditschek, Biologically inspired climbing with a hexapedal robot. *J. Field Robot.* **25**, 223–242 (2008).
17. G. C. Haynes, A. Khripin, G. Lynch, J. Amory, A. Saunders, A. A. Rizzi, D. E. Koditschek, Rapid pole climbing with a quadrupedal robot, in *IEEE International Conference on Robotics and Automation* (IEEE, 2009), pp. 2767–2772.
18. P. Birkmeyer, A. G. Gillies, R. S. Fearing, Clash: Climbing vertical loose cloth, in *IEEE/RSJ International Conference on Intelligent Robots and Systems* (IEEE, 2011), pp. 5087–5093.
19. G. A. Lynch, J. E. Clark, P.-C. Lin, D. E. Koditschek, A bioinspired dynamical vertical climbing robot. *Int. J. Rob. Res.* **31**, 974–996 (2012).
20. S. D. de Rivaz, B. Goldberg, N. Doshi, K. Jayaram, J. Zhou, R. J. Wood, Inverted and vertical climbing of a quadrupedal microrobot using electroadhesion. *Sci. Robot.* **3**, eaau3038 (2018).
21. H. Prahlad, R. Pelrine, S. Stanford, J. Marlow, R. Kornbluh, Electroadhesive robots—Wall climbing robots enabled by a novel, robust, and electrically controllable adhesion

technology, in *IEEE International Conference on Robotics and Automation* (IEEE, 2008), pp. 3028–3033.

22. F. Rochat, R. Beira, H. Bleuler, F. Mondada, Tremo: An inspection climbing inchworm based on magnetic switchable device, in *Field Robotics* (World Scientific, 2012), pp. 421–428.
23. P. Ward, P. Manamperi, P. Brooks, P. Mann, W. Kaluarachchi, L. Matkovic, G. Paul, C. Yang, P. Quin, D. Pagano, D. Liu, K. Waldron, G. Dissanayake, Climbing robot for steel bridge inspection: Design challenges, in *Austroads Bridge Conference* (ARRB Group, 2014), pp. 1–13.
24. H. Sison, P. Ratsamee, M. Higashida, T. Mashita, Y. Uranishi, H. Takemura, Spherical magnetic joint for inverted locomotion of multi-legged robot, in *IEEE International Conference on Robotics and Automation* (IEEE, 2021), pp. 1170–1176.
25. J. C. Grieco, M. Prieto, M. Armada, P. G. De Santos, A six-legged climbing robot for high payloads, in *IEEE International Conference on Control Applications* (IEEE, 1998), vol. 1, pp. 446–450.
26. Z. Bi, Y. Guan, S. Chen, H. Zhu, H. Zhang, A miniature biped wall-climbing robot for inspection of magnetic metal surfaces, in *IEEE International Conference on Robotics and Biomimetics* (IEEE, 2012), pp. 324–329.
27. T. Arai, K. Kamiyama, P. Kriengkomol, Y. Mae, M. Kojima, M. Horade, Inspection robot in complicated 3D environments, in Proceedings of the 32nd International Symposium on Automation and Robotics in Construction, Oulu, Finland, 15 to 18 June 2015, vol. 32, pp. 1–6.
28. T. Bandyopadhyay, R. Steindl, F. Talbot, N. Kottege, R. Dungavell, B. Wood, J. Barker, K. Hoehn, A. Elfes, Magneto: A versatile multi-limbed inspection robot, in *IEEE/RSJ International Conference on Intelligent Robots and Systems* (IEEE, 2018), pp. 2253–2260.
29. P. Kriengkomol, K. Kamiyama, M. Kojima, M. Horade, Y. Mae, T. Arai, A new close-loop control method for an inspection robot equipped with electropermanent-magnets. *J. Robot. Mechatron.* **28**, 185–193 (2016).
30. S. Seok, A. Wang, D. Otten, S. Kim, Actuator design for high force proprioceptive control in fast legged locomotion, in *IEEE/RSJ International Conference on Intelligent Robots and Systems* (IEEE, 2012), pp. 1970–1975.
31. P. M. Wensing, A. Wang, S. Seok, D. Otten, J. Lang, S. Kim, Proprioceptive actuator design in the MIT cheetah: Impact mitigation and high-bandwidth physical interaction for dynamic legged robots. *IEEE Trans. Robot.* **33**, 509–522 (2017).
32. Y. Ding, H.-W. Park, Design and experimental implementation of a quasi-direct-drive leg for optimized jumping, in *IEEE/RSJ International Conference on Intelligent Robots and Systems* (IEEE, 2017), pp. 300–305.
33. A. N. Knaian, "Electropermanent magnetic connectors and actuators: Devices and their application in programmable matter," thesis, Massachusetts Institute of Technology, Cambridge, MA (2010).
34. P. Ward, D. Liu, Design of a high capacity electro permanent magnetic adhesion for climbing robots, in *IEEE International Conference on Robotics and Biomimetics* (IEEE, 2012), pp. 217–222.
35. A. D. Marchese, C. D. Onal, D. Rus, Soft robot actuators using energy-efficient valves controlled by electropermanent magnets, in *IEEE/RSJ International Conference on Intelligent Robots and Systems* (IEEE, 2011), pp. 756–761.
36. J. I. Padovani, S. S. Jeffrey, R. T. Howe, Electropermanent magnet actuation for droplet ferromicrofluidics. *Dent. Tech.* **4**, 110–119 (2016).
37. A. Gholizadeh, S. Abbaslou, P. Xie, A. Knaian, M. Javanmard, Electronically actuated microfluidic valves with zero static-power consumption using electropermanent magnets. *Sens. Actuators A Phys.* **296**, 316–323 (2019).
38. K. Autumn, S. T. Hsieh, D. M. Dudek, J. Chen, C. Chitaphan, R. J. Full, Dynamics of geckos running vertically. *J. Exp. Biol.* **209**, 260–272 (2006).
39. H.-W. Park, P. M. Wensing, S. Kim, High-speed bounding with the MIT cheetah 2: Control design and experiments. *Int. J. Rob. Res.* **36**, 167–192 (2017).
40. B. Katz, J. Di Carlo, S. Kim, Mini cheetah: A platform for pushing the limits of dynamic quadruped control, in *International Conference on Robotics and Automation* (IEEE, 2019), pp. 6295–6301.
41. C. Semini, V. Barasuol, M. Focchi, C. Boelens, M. Emara, S. Casella, O. Villarreal, R. Orsolino, G. Fink, S. Fahmi, G. A. Medrano-Cerda, D. G. Caldwell, Brief introduction to the quadruped robot hyqreal, in Italian Conference on Robotics and Intelligent Machines, Rome, Italy, 18 to 20 October 2019.
42. M. Hutter, C. Gehring, D. Jud, A. Lauber, C. D. Bellicoso, V. Tsounis, J. Hwangbo, K. Bodie, P. Fankhauser, M. Bloesch, R. Diethelm, S. Bachmann, A. Melzer, M. Hoepflinger, ANYmal-a highly mobile and dynamic quadrupedal robot, in *IEEE/RSJ International Conference on Intelligent Robots and Systems* (IEEE, 2016), pp. 38–44.
43. Spot autonomous navigation; https://youtu.be/Ve9kWX_KXus [accessed 20 May 2022].
44. J. M. Ginder, M. E. Nichols, L. D. Elie, J. L. Tardiff, Magnetorheological elastomers: Properties and applications, in *Smart Structures and Materials 1999: Smart Materials Technologies* (SPIE, 1999), vol. 3675, pp. 131–138.
45. Y. Li, J. Li, W. Li, H. Du, A state-of-the-art review on magnetorheological elastomer devices. *Smart materials and structures* **23**, 123001 (2014).
46. T. Liu, Y. Xu, Magnetorheological elastomers: Materials and applications, in *Smart and Functional Soft Materials* (Books on Demand, 2019), pp. 147–180.
47. A. K. Bastola, M. Paudel, L. Li, Magnetic circuit analysis to obtain the magnetic permeability of magnetorheological elastomers. *J. Intell. Mater. Syst. Struct.* **29**, 2946–2953 (2018).
48. W. H. Hayt Jr., J. A. Buck, Appendix C, in *Engineering Electromagnetics* (McGraw-Hill, ed. 8, 2010), pp. 564.
49. H.-W, Park, P. Wensing, S. Kim, Online planning for autonomous running jumps over obstacles in high-speed quadrupeds, in *Proceedings of Robotics: Science and Systems* (RSS, 2015), pp.1–9.
50. J. Di Carlo, P. Wensing, B. Katz, G. Bledt, S. Kim, Dynamic locomotion in the MIT cheetah 3 through convex model-predictive control, in *IEEE/RSJ International Conference on Intelligent Robots and Systems* (IEEE, 2018), pp. 1–9.
51. Y. Ding, A. Pandala, C. Li, Y. Shin, H.-W. Park, Representation-free model predictive control for dynamic motions in quadrupeds. *IEEE Transact. Robot.* **37**, 1154–1171 (2021).
52. A. Agrawal, S. Chen, A. Rai, K. Sreenath, Vision-aided dynamic quadrupedal locomotion on discrete terrain using motion libraries, in *IEEE International Conference on Robotics and Automation* (IEEE, 2022), pp. 4708–4714.
53. Y. Shin, S. Hong, S. Woo, J. Choe, H. Son, G. Kim, J. Kim, K. Lee, J. Hwangbo, H.-W. Park, Design of KAIST HOUND, a quadruped robot platform for fast and efficient locomotion with mixed-integer nonlinear optimization of a gear train, in *IEEE International Conference on Robotics and Automation* (IEEE, 2022), pp. 6614–6620.
54. S. Hong, J.-H. Kim, H.-W. Park, Real-time constrained nonlinear model predictive control on SO(3) for dynamic legged locomotion, in *IEEE/RSJ International Conference on Intelligent Robots and Systems* (IEEE, 2021), pp. 3982–3989.
55. M. H. Raibert, in *Legged Robots that Balance* (MIT Press, 1986), vol. 1, 89 pp.
56. J. Pratt, C. Chew, A. Torres, P. Dilworth, G. Pratt, Virtual model control: An intuitive approach for bipedal locomotion. *Int. J. Rob. Res.* **20**, 129–143 (2001).
57. Improve shipyard welding with miller arcreach technology; www.youtube.com/watch?v=Siz4mQZlRq4 [accessed 20 May 2022].
58. Crews inspect golden gate bridge towers; www.youtube.com/watch?v=9R3vtpJApfk [accessed 20 May 2022].
59. J. E. Japka, Microstructure and properties of carbonyl iron powder. *JOM* **40**, 18–21 (1988).
60. W. D. Shin, J. Park, H.-W. Park, Development and experiments of a bio-inspired robot with multi-mode in aerial and terrestrial locomotion. *Bioinspir. Biomim.* **14**, 056009 (2019).
61. R. C. Hibbeler, *Mechanics of Materials* (Pearson, ed. 10, 2015).
62. A. J. Bombard, I. Joekes, M. R. Alcântara, M. Knobel, Magnetic susceptibility and saturation magnetization of some carbonyl iron powders used in magnetorheological fluids, in *Materials Science Forum* (Trans Tech Publication, 2003), vol. 416–418, p. 753.

Acknowledgments

We would like to thank Y. Ding, C. Li, and H. Son for their work in design of leg modules and electronics. We also thank D. Kang for work in the MARVEL locomotion experiment and G. Han and S. Kang for support in magnetic holding force measurement. **Funding:** The project was supported by Korea Shipbuilding & Offshore Engineering (KSOE), the National Research Foundation of Korea (NRF) (NRF-2022R1A2C2011927), and the Department of Mechanical Engineering, Korea Advanced Institute of Science and Technology (KAIST). **Author contributions:** S.H., Y.U., and J.P. were the main contributors to the project. S.H., Y.U., and H.-W.P. led the experimental work. Y.U. and J.P. contributed in design, manufacture, and fabrication of the S-EPM, MRE, magnetic foot, and MARVEL. S.H. implemented the robot software including locomotion control framework. H.-W.P. conceived the main idea and supervised the work. **Competing interests:** The authors declare that they have no competing interests. **Data and materials availability:** All data needed to support the conclusions of this manuscript are included in the main text or Supplementary Materials.

Submitted 20 May 2022
Accepted 17 November 2022
Published 14 December 2022
10.1126/scirobotics.add1017

Science Robotics

Agile and versatile climbing on ferromagnetic surfaces with a quadrupedal robot

Seungwoo Hong, Yong Um, Jaejun Park, and Hae-Won Park

Sci. Robot. **7** (73), eadd1017. DOI: 10.1126/scirobotics.add1017

Science Robotics (ISSN 2470-9476) is published by the American Association for the Advancement of Science. 1200 New York Avenue NW, Washington, DC 20005. The title *Science Robotics* is a registered trademark of AAAS.